Cold Regions Science and Technology 221 (2024) 104157

Contents lists available at ScienceDirect

Cold Regions Science and Technology

journal homepage: www.elsevier.com/locate/coldregions

A laser ultrasound system to non-invasively measure compression waves in granular ice mixes

J. Chris McCaslin [a,*], T. Dylan Mikesell [b], Hans-Peter Marshall [a]

[a] Boise State University, Boise, ID, USA
[b] Norwegian Geotechnical Institute, Oslo, Norway

ARTICLE INFO

Keywords:
Laser ultrasonics
Snow density
Compression waves
Poro-elastic waves

ABSTRACT

Accurate knowledge of snow mechanical properties, including Young's modulus, shear modulus, Poisson's ratio, and density, is critical to many areas of snow science and to snow-related engineering problems. To facilitate the assessment of these properties, an innovative non-contacting laser ultrasound system (LUS) has been developed. This system acquires ultrasound waveform data at frequencies ranging from tens to hundreds of kHz in a controlled cold-lab environment. Two different LUS devices were compared in this study to determine which recorded more robust ultrasound in granular ice mix samples. We validated the ultrasound observations with poro-elastic traveltime modeling based on physical and empirical constitutive relationships, comparison to and replication of previous studies, and the use of other accredited snow property measurement systems, i.e., the SnowMicroPen. For ice mixes, we determined that the PSV-400 Scanning Vibrometer (Polytec GmbH) produces higher quality ultrasonic wavefield observations (i.e. has a better signal-to-noise ratio) than the VibroFlex Fiber Vibrometer (Polytec GmbH) in the lab conditions tested here. Using the PSV-400, we then demonstrated the utility of this new LUS to study the relationship between snow compression-wave speed and density during snow compaction experiments.

1. Introduction

For decades researchers have worked to develop in situ and remote sensing techniques to infer snow density, as well as various other microstructural and mechanical snow properties (e.g., Lowe and Herwijnen, 2012; McGrath et al., 2022). However, still today many of these properties remain difficult to quantify. The mechanical properties used to describe snow include Young's modulus, Poisson's ratio, bulk modulus, and shear modulus. For vehicle mobility, data on snow surface strength is necessary to infer the maximum overburden stress the snow can withstand (Sopher and Shoop, 2017, Shoop et al., 2020). These are critical properties that need to be accurately assessed over large temporal and spatial scales to enable useful stability analyses over a snowpack (e.g., avalanche forecasting or determination of mobility potential). Microstructural properties can include porosity, snow crystal type, or specific surface area, which plays an essential role in radar-based remote sensing estimates of snow water equivalent (SWE) – total equivalent amount of water contained in the snow. For SWE calculations, density is another crucial parameter; density is multiplied by the snow depth to calculate SWE in a snow column. Unfortunately, no one method, or even a suite of methods, has yet been developed that can provide information about all these important properties at once for the same snow sample or snowpack. Furthermore, despite significant advances in observational technology, natural snow is incredibly complex and seasonal snowpacks have significant spatial and temporal variability, which means many observations through space and time are required to accurately characterize a snowpack.

There are many snow properties that have been characterized using geophysical, remote sensing, or optical methods. Remote sensing techniques are well suited to characterize spatial variability, while tower-based observation techniques are often more well suited to study the temporal variability (e.g., Ruiz et al., 2020; Stefko et al., 2022). Previous research on mechanical properties has been limited (e.g., Shapiro et al., 1997), which presents an opportunity for ground-based methods that observe or can infer snow mechanical properties (e.g., seismic methods, Hofstede et al., 2013; Brucker et al., 2011). Past studies have used acoustic waves to characterize snow via observations of wave propagation and attenuation in snow (e.g., Oura, 1952; Ishida, 1965; Yamada et al., 1974), the acoustic response of snow in avalanche mitigation (e.g., Gubler, 1977), the stability of a natural snowpack (e.g., Gubler, 1983),

* Corresponding author.
E-mail address: chrismccaslin@u.boisestate.edu (J.C. McCaslin).

https://doi.org/10.1016/j.coldregions.2024.104157
Received 3 October 2023; Received in revised form 27 January 2024; Accepted 26 February 2024
Available online 11 March 2024

avalanche monitoring (e.g., Surinach et al., 2001; Herwijnen and Schweizer, 2011; Lacroix et al., 2012), and the estimation of snow water equivalent (SWE) (e.g., Kinar and Pomeroy, 2009; Lieblappen et al., 2020). Optical and microwave (orbital) remote sensing techniques can provide information about the surface grain size (e.g., Tsang et al., 2022; Picard et al., 2022), but normally these non-contacting methods cannot be used to observe mechanical or microstructural properties directly. Moreover, beyond stationary active or passive in situ measurements, most field-based observations of snowpacks (e.g., snow pits) are invasive and damage snow integrity, inhibiting the ability to revisit a sample in time or use additional instruments to characterize all properties of the same sample.

Mechanical waves are sensitive to the microstructural and mechanical properties of elastic and poro-elastic materials, making it a potential technique to measure relevant snow properties in a non-destructive manner in the lab, and the application of ultrasound (i.e., high-frequency mechanical wave propagation) to snow is not novel in itself (e.g., Oura, 1952; Smith, 1965; Ishida, 1965; Yamada et al., 1974; Marco et al., 1998; Iwase et al., 2001; Takei and Maeno, 2004; Gudra and Najwer, 2011; Reiweger et al., 2015; Capelli et al., 2016; Lieblappen et al., 2020). Past research on snow using ultrasound has largely consisted of contacting sensors and/or piezoelectric transducers coupled to snow samples or the snowpack (e.g., Kapil et al., 2014; Reiweger et al., 2015; Capelli et al., 2016). Laboratory-scale mechanical wave experiments often use ultrasonic rather than seismic or infrasound frequencies to probe the mechanical properties of small-scale representative samples. For example, reflected and transmitted acoustic waves in porous materials can be used to deduce mechanical and microstructural properties (e.g., pore size and its distribution, porosity, and density) within an inverse scattering framework (Fellah et al., 2003a).

Few studies have used non-invasive and non-contacting techniques to study snow and ice cores using ultrasonic wavefields (e.g., Mikesell et al., 2017; Lieblappen et al., 2020). These studies demonstrate that a laser ultrasound system (LUS) is conducive to observe microstructural components that are often not observable without destruction of the sample. Additionally, due to the difficulty of measuring ultrasound in snow, multiple studies previously analyzed analogue porous materials (e.g., sintered glass beads, porous metals, or ceramics), assuming their mechanical properties and microstructure are similar to snow (e.g., Mason and Thurston, 1972; Fellah et al., 2003a, 2003b). What is fundamentally difficult about snow is that it changes over time through different dynamic processes, namely ablation and metamorphism. Thus, these analogue materials often provide only one type of representative analogue (a snapshot of reality) and do not capture the wide range of snow properties known to exist in nature.

Thus, there is a real need for more studies on actual snow from the lens of ultrasound observations. Capelli et al. (2016) compiled various observations of mechanical wave speed as a function of snow density. Capelli et al. (2016) used a poro-elastic model (i.e., Biot's model) to synthesize these data, which can contain multiple compression wave phases (i.e., the slow and fast P waves) and the shear (S) wave phases. Building on the work of Sidler (2015), which provides an empirical relationship linking density, porosity, and elastic waves speed via Krief's equation and an effective Poisson's ratio, Capelli et al. (2016) built an empirical poro-elastic relationship between snow density and compression- (P) and shear-wave (S) speed. To interpret the wave speeds in this way, it is assumed that the propagation of the waves in a porous snowpack is sensitive to the elastic solid phase (i.e., ice) and the viscous fluid/gas phase (i.e., air). Capelli et al. (2016) validated this relationship using data from a novel contacting piezoelectric acoustic-pulse experiment.

In this study we further investigate snow density through the lens of ultrasound, but using a novel non-contacting LUS we have developed for laboratory study of snow. In addition to using the PSV-400 Scanning Vibrometer that already exists within our lab (e.g., Mikesell et al., 2017), we rented a VibroFlex Fiber LUS interferometer so that we could compare the signal-to-noise ratio of the two sensors on artificial snow samples (i.e., fine shaved ice crystals). We provide a comprehensive comparison of ultrasonic wavefield observations for varying ice crystal densities and interpret the corresponding changes in seismic compression wave speeds observed with the LUS. Following Capelli et al. (2016), we use the theory provided in Sidler (2015) to interpret this new dataset, whereby we estimate porosity and density by combining the Biot model for porous snow (Capelli et al., 2016) with the model of (Sidler, 2015) to link everything via Poisson's ratio and Krief's equation (Section 2.1). Given that Capelli et al. (2016) compiled past data sets of compression and shear wave speeds in snow with various densities, we place our new observations on shaved ice within this context and compare to past studies of snow. We summarize the comparison of the two the lasers and results of the compaction experiments in Section 3. We discuss (Section 4) how this type of ultrasound data can be used to further validate or modify these types of empirical relationships between ultrasound and snow microstructural and mechanical properties (i.e., density, Young's modulus, shear modulus, Poisson's ratio, etc). By developing this system, we set the stage for future LUS research into these important snow properties. This novel system will enable the study of snow at different temperatures and liquid water saturations, snow of different crystal structures, and snow that has endured different environmental conditions and thus metamorphism.

2. Materials and methods

2.1. Poro-elastic wave observations in snow

To enable the study of different constitutive relationships under varying snow conditions, we have developed a non-contacting LUS to study snow samples in a cold lab environment. Here, we study the P-wave speed and density relationship and use a non-linear empirical model shown in Capelli et al. (2016) and Sidler (2015) to validate our new observations. This model assumes dry snow only. We first review this model and then describe how we apply it in this study.

Sidler (2015) presents a comprehensive overview of a poro-elastic model that uses an empirical Biot model to link snow density (ρ_s), porosity ($\varnothing$), Poisson's ratio (ν), and bulk modulus (K_m). The first step is to relate porosity to snow density:

$$\varnothing = 1 - \frac{\rho_s}{916.8} \tag{1}$$

where 916.8 kg/m^3 is the density of ice. Most porous materials have a so-called critical porosity ($\varnothing_c$), which dis- tinguishes two distinct domains of acoustic behavior (Mavko et al., 2020). For porosity below $\varnothing_c$ the solid frame is load-bearing and for porosity above $\varnothing_c$ the porous material acts like a suspension of solids. Snow has a high critical porosity (~0.8), similar to pumice (Sidler, 2015). The Krief equation is often used in rock physics as it combines the two porosity ranges (e.g., Carcione and Picotti, 2006). Thus, Sidler (2015) uses the Krief equation to calculate the bulk modulus (K_m) of snow as a function of porosity:

$$K_m = 10000(1 - \varnothing)^{30.85/(7.76-\varnothing)} \tag{2}$$

where the coefficients in the exponent of the Krief equation come from a least-squares fit to the measurements presented in Johnson (1982). Sidler (2015) also provides a linear relationship between Poisson's ratio and porosity that matches well past measurements (e.g., Smith, 1969):

$$\nu = 0.38 - (0.36\varnothing) \tag{3}$$

Having relationships for Poisson's ratio and the bulk modulus, we can compute Young's modulus (E):

$$E = (K_m - 2\nu) \tag{4}$$

and the corresponding P- and S-wave phase speeds, c_p and c_s respectively, for poro-elastic materials (e.g., Capelli et al., 2016):and

$$c_p = \sqrt{\frac{E(1-v)}{\rho_s(1-v)(1-2v)}} \tag{5}$$

$$c_s = \sqrt{\frac{E}{2\rho_s(1-v)}} \tag{6}$$

Note here that we are considering the *fast* P wave, i.e., the compression wave in the poro-elastic medium that propagates through the rigid skeletal frame, not the *slow* wave which propagates through the pore space in the fluid. Taking that into account, we observe that all parameters that go into the wave speed equations depend on porosity, which in turn depends on density. Thus, we compute the wave speed as a function of density (Fig. 1), and our goal is now to demonstrate that we can collect equivalent wave speed data using the non-contacting LUS with shaved ice samples with varying densities.

2.2. Experimental setup

We created samples of granular ice by first shaving ice blocks into fine ice crystals. Then we gently poured the crystals into a steel cylinder (Fig. 2a) with known dimensions and measured the initial mass of the granular ice mix using a digital scale. To create snow samples with different densities, we compacted the grains within the steel cylinder at intervals of approximately 0.5 cm using a custom-made compaction apparatus (Fig. 2b), where compaction is defined as the distance from the top of the cylinder (9 cm) to the compacted snow surface. After compaction, we slide the steel cylinder up and off the snow sample, resulting in a cylindrical snow sample with a density profile that can either be assumed homogeneous or can vary with depth along the vertical axis of the cylinder.

2.2.1. Snow density measurement

Knowing the bulk density of the snow sample (ρ_s) is critical in this study. Two methods are used to obtain density estimates of compacted artificial snow samples: (1) calculation of the gravimetric snow density using the volume and mass of the snow sample and (2) inference of density from measurements with the Snow MicroPenetrometer (SnowMicroPen or SMP). The SMP measures the penetration force and strength of the bonded snow structure, records the force required to break through snow crystal bonds, and builds a vertical profile along the penetration path (Schneebeli and Johnson, 1999). Penetration data are inverted using software from Swiss Federal Institute (WSL) for Snow and Avalanche Research (SLF) to obtain density estimates (Grimm et al., 2018).

In contrast to the SMP method, the height and diameter of the snow sample are used to calculate the volume. With the measured mass of the sample, gravimetric snow density of a compacted sample (ρ_{sc}) is calculated by dividing the mass by the volume of the snow sample:

$$\rho_{sc} = \frac{m}{\pi r^2 (h - c_i)} \tag{7}$$

with m the mass of the snow sample without the steel cylinder (in kilograms), r the radius of the snow sample (in meters), h the height of the snow sample (in meters), and c_i the compaction measurement from the top (in meters).

2.2.2. The cold lab

The cold lab is from BioCold Environmental Inc., and it provides humidity and temperature control, with two independent cooling systems to provide stable temperature during defrost cycles. The temperature can be adjusted from −40 to 60 °C with a refrigeration system that maintains temperature control of ±0.3 °C. In this experiment the lab is kept at −20 °C.

2.2.3. Laser system

We use the LUS to probe a snow sample with acoustic waves. This system enables us to directly measure the normal particle motion at the

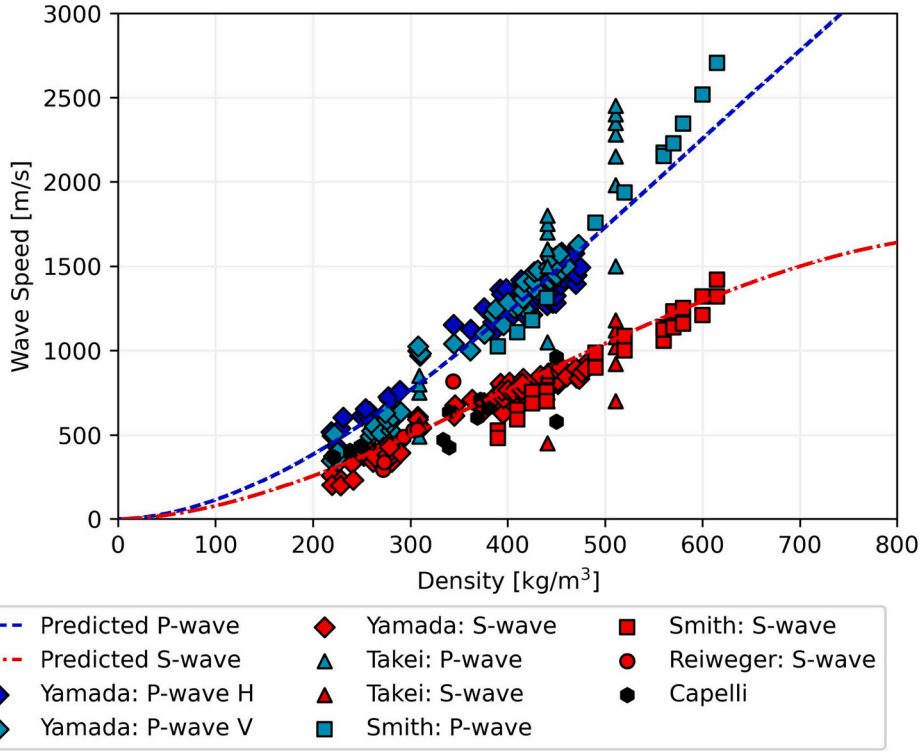

Fig. 1. Past wave speed-density data compiled by Capelli et al. (2016): P-waves (blue) and S-waves (red). The dashed blue line is the predicted P-wave speed-density relationship from Eq. (5) and the dashed red line is the predicted S- wave speed-density relationship from Eq. (6). See Capelli et al. (2016) for a discussion of the different P- and S-wave datasets. (For interpretation of the references to colour in this figure legend, the reader is referred to the web version of this article.)

(a) (b)

Fig. 2. a) Photo of the steel cylinder used for compaction. b) Photo of the compaction apparatus used to compact snow within the steel cylinder.

snow sample surface as an ultrasonic wave passes by and deforms the surface. The laser ultrasound system consists of one source and one receiver laser (e.g., Mikesell et al., 2017). The source laser excites the snow sample. We use a 1064 nm Nd:YAG (yttrium aluminum garnet) laser, model INDI from Spectra- Physics. The source laser pulses energy up to 450 mJ with durations from 6 to 9 ns. The pulse repetition rate is set to 10 Hz. The radiation emitted from the source laser is absorbed at the surface of the snow sample where the laser is pointed. This absorption causes rapid heating and thermal energy then propagates into the sample as thermal waves. The pulsed heating is in short intervals, so this does not cause melting of the sample. The heated region undergoes thermal expansion whereby the associated thermo-elastic stresses and strains act as a small ultrasonic source, creating ultrasonic waves that propagate throughout the snow sample (Scruby and Drain, 1990).

The propagated ultrasonic waves can be recorded on the surface of the sample by one of two laser systems: an optical interferometer (Scruby and Drain, 1990; Hariharan, 2006) or an optical vibrometer (Scruby and Drain, 1990). In this study, we test two receiver laser systems to determine if one is more suited than the other for studies of snow. The first is a Polytec PSV-400 Scanning Vibrometer (PSV) and the second is Polytec VibroFlex Fiber (PVF), an interferometry-based system. Both laser systems have a linear frequency response from the acoustic range to the high ultrasonic range. Both laser systems are composed of three parts: the acquisition software, the workstation and laser head. The laser is emitted from the laser head, back-scattered off the surface of interest to the sensor within the head, and mixed with the reference signal to provide a time series of the particle velocity at the spot where the laser reflects on the sample surface. We use the surface-particle velocity to determine when the elastic wave arrives (e.g., Mikesell et al., 2017). The Polytec software controls the laser, triggers the source, and enables further data processing and visualization. The workstation contains the laser controller, the data management system, and connects the sensor head and source laser for triggering. This simultaneous triggering of the source and receiver lasers enables stacking multiple acquisitions to reduce the ambient noise from the cold room and improve the signal-to-noise ratio (SNR).

The PSV sensor head contains the laser (a HeNe laser – 633 nm wavelength), the scanning unit, and a video camera to display the scanning area within the software. The PSV specifications that need to be considered when running the laser are shown in Table 1. The PVF sensor head contains the fiber optic cable acting as the laser sensor head (which is also a HeNe laser – 633 nm wavelength, Polytec, 2022). The VibroFlex Connect is the control mechanism used to adjust the data acquisition parameters and specifications (Table 1). Both laser heads work best when the laser beam intersects perpendicular to the sample surface as this provides the best reflectance. Based on Table 1, it is apparent that the PSV-400 provides more breadth in terms of recording options. For example, the distance from the laser head to the snow sample surface (i.e., the standoff distance) is much larger for the PSV-400, the maximum particle velocity from the moving surface is greater for the PSV-400, and the PSV-400 has auto focus capability. That said, we rented and tested the PVF because we wanted to determine if using the fiber head provided any advantages in terms of acquisition setup.

The two laser systems vary somewhat in their setup relative to the cold lab and the sample. On one side of the sample, the receiver laser measures the ultrasonic wavefield, while on the opposite side the source laser excites the ultrasonic waves. The source laser is positioned outside the cold lab, with the beam pointing at the snow sample and traveling through a sapphire window into the cold lab. This general setup describes an ultrasound transmission experiment, and the systems vary only on the receiver side of the experiment, which is largely to prevent

Table 1
Polytec PSV-400 scanning vibrometer and polytec VibroFlex vibrometer specifications.

Speciffcation	PSV-400 (PSV)	VibroFlex (PVF)
Bandwidth	DC to 20 MHz	DC to 24 MHz
Standoff Distance	0.4 m – 100 m	0.005 m – 0.06 m
Laser Type	Helium Neon (HeNe)	Helium Neon (HeNe)
Laser Wavelength	633 nm	633 nm
Focus	Auto Focus	Manual Focus
Grid Size	512 × 512	1 × 1
Operating Temperature	5 °C – 40 °C	5 °C – 40 °C
Maximum Particle Velocity	20 m/s	12 m/s
Trace Stacking	100 Samples	100 Samples
Sample Rate	1.28 MHz	1.28 MHz
T_{max}	399.2 μs	399.2 μs

damage to the PVF.

For the PSV system, the receiver laser is positioned entirely outside the cold lab. The laser beam travels through another sapphire window into the cold lab (Fig. 3a). These optical sapphire windows installed in the cold lab walls have a viewing dimension of 32.4 cm by 32.4 cm and are 2.5 cm thick. The windows consist of three pieces of tempered glass (Mikesell et al., 2017), and sapphire is used because it is mostly transparent to the beam. The windows are made by Norfab Inc. and are called Vu-Port.

Compared to the PSV setup, the PVF system differs in terms of the receive laser location. The PVF receiver laser is positioned outside of the cold lab, and the fiber optic head is fed through a tube with the end of the fiber placed right at the interior end of the tube, 0.02 m from the snow sample (Fig. 3b). This is required due to the difference in standoff distance and manual focus compared to the PSV. In addition to needing to be close the sample surface, the PVF fiber optic head should not reach below 0° C or we risk damaging the components. Thus, this setup actually allows air to mix between the cold lab and outside, causing some wind in the tunnel and leading to noise (i.e., unwanted vibration in the laser head). Thus, we anticipate that the two systems could have different SNRs purely related to the acquisition system.

2.3. Experiment 1: PSV vs. PVF

The standoff distance from the PSV to the snow sample is approximately 0.45 m and 0.02 m for the PVF. Mikesell et al. (2017) demonstrate that a reflective tape needs to be applied to ice samples to get sufficient reflectance for the PSV to record the wavefield. Because of

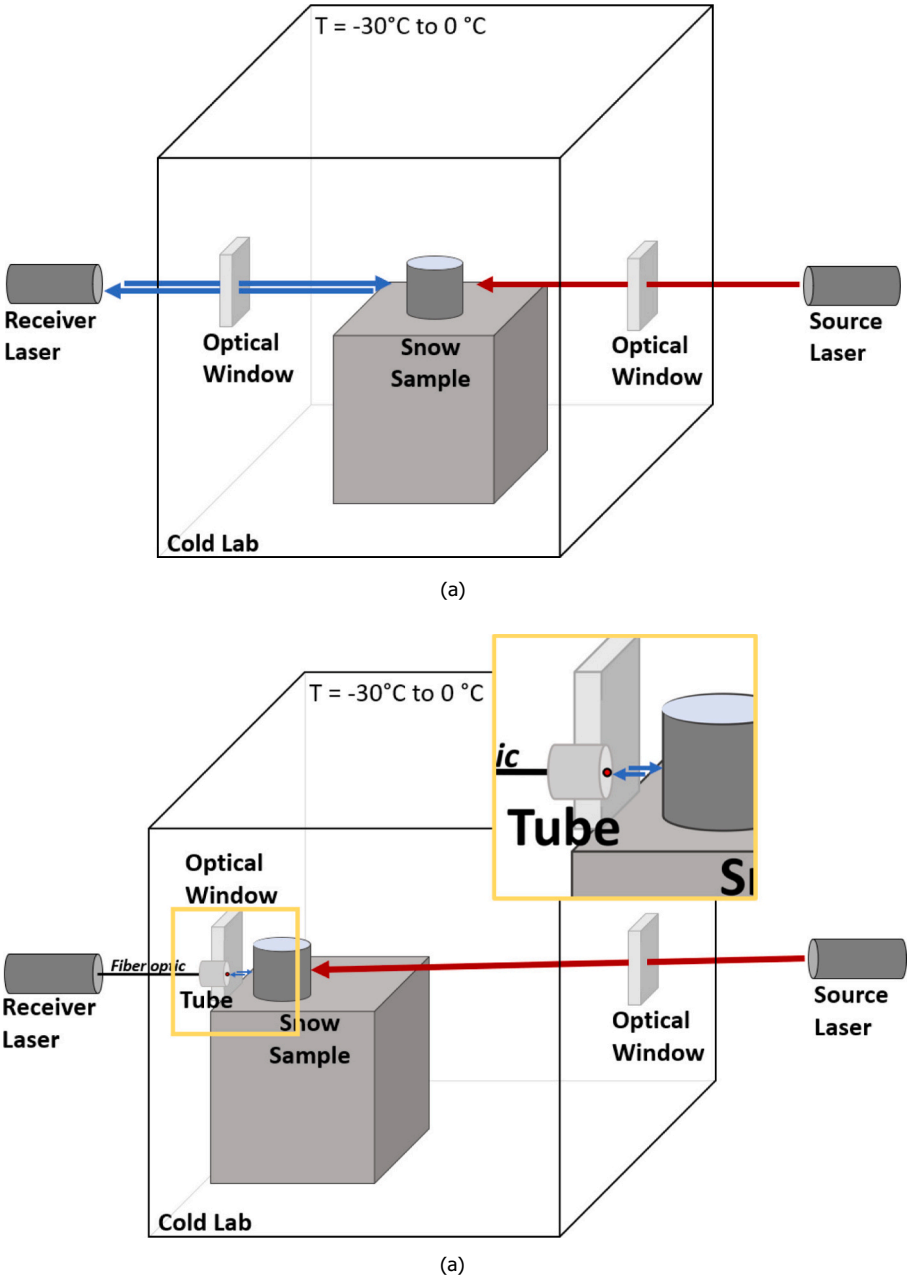

Fig. 3. a) Laser ultrasound system: PSV receiver laser, Nd:YAG source laser, and snow sample inside cold lab. The blue arrow indicates the receiver laser beam reflecting perpendicular to the sample surface. The red arrow indicates the source laser on the opposite side of the snow sample. The lasers access the sample through the optical windows. b) Same as (a), but with PVF receiver laser. The blue arrow indicates the receiver laser beam through the tube in cold lab wall (inset). (For interpretation of the references to colour in this figure legend, the reader is referred to the web version of this article.)

this, two experiments were conducted for each receiver laser on the snow sample, one with reflective tape and one without reflective tape. This experiment is used to determine if reflectance from the snow surface is sufficient for either laser or if reflective tape is necessary for snow, as it was in ice cores. Thus, prior to recording data, the reflection of scattered laser light from the receiver was maximized by focusing each laser on the snow sample surface at the respective standoff distances.

The acquisition software has an auto-focus feature when using the PSV. This is because the standoff distance can vary and the PSV laser head is more sophisticated in terms of hardware capabilities. Prior to PVF acquisition, additional hardware (the VibroFlex Connect) is needed to tune the PVF parameters. The PVF connects to the VibroFlex Connect which then connects to the acquisition software. VibroFlex Connect is similar to the acquisition software in terms of being able to set parameters for the PVF, as well as view the backscatter reflectance level; however, there is no auto-focus feature for the PVF. Thus, the PVF head has to be manually focused by turning the head while maintaining the same laser spot on the snow sample surface. This is an additional challenge of the PVF compared to the PSV.

For both the receiver laser setups, 100 traces are averaged to reduce the random noise in the data. Other acquisition parameters are displayed in Table 1. Once an averaged trace is acquired, the raw data are displayed in the frequency domain within the Polytec Display software. For further processing, visualization, and interpretation, the data are converted to the time domain using the inverse FFT function in the display software. Additionally, a PVF signal advance of 40 μs is applied before interpretation; this is to correct for a systematic hardware delay. The value of this delay is provided by Polytec and depends on the acquisition sample rate, 1.28 MHz in this case. To highlight the signal of interest, a 3–300 kHz zero-phase 2nd-order Butterworth bandpass filter is applied using Python. Prior to filtering a cosine taper is applied to the first and last 30% of each trace to prevent edge effects. To determine which receiver has the higher SNR in the selected frequency band we calculate the SNR by computing the root mean square (RMS) value of the ultrasound (i.e., the signal after the first arrival) and dividing this by the root mean square (RMS) value of the noise (i.e., the signal prior to the first arrival).

2.4. Experiment 2: snow compaction

To determine if we can observe density-related ultrasound wave speed changes, we conduct a snow compaction experiment. We compact a lab-made snow sample and then complete a transmission experiment using the PSV system, anticipating that we should observe systematic increases in the P-wave speed from increasing Poisson's ratio and Young's modulus by decreasing porosity (i.e., Section 2.1). The P-wave arrival time is estimated from the processed PSV time series and converted to P-wave speed using the snow sample diameter. The SMP is used to determine the density of each snow sample (Fig. 4), in addition to calculating gravimetric density based on mass and volume. The SMP requires that the penetration rod is oriented normal to the snow surface, which also prevents damage to the instrument. A wooden frame was built (Fig. 4a) to hold the SMP perpendicular to the snow surface and maintain a constant height above the snow sample. The SMP is secured on top of the wooden structure and the experiment is controlled using the interface connected to the SMP. Three vertical SMP profiles are collected after each compaction experiment to interrogate the spatial variability (Fig. 4b). Each SMP profile is saved on a SD card as a .PNT file. The data are transferred to a desktop and the penetration force data are used to estimate the density along the profile in 1 mm increments. Python is used for processing and the software is provided by SLF (Grimm et al., 2018).

3. Results

3.1. PSV vs. PVF

The raw and processed ultrasound time series produced by the PSV and the PVF are displayed in Fig. 5. Four traces are compared: both laser systems with and without reflective tape. It is apparent that the traces with the reflective tape contain coherent and consistent ultrasound records for both lasers, at least in the first-arrival sense (Fig. 5a and c). It is also apparent that the traces without the reflective tape do not contain coherent ultrasound arrivals (Fig. 5b and d). In fact, if you compare the particle velocity amplitudes for the traces without tape, you note that the amplitudes are much larger compared to the traces with tape. One then asks, has the noise increased and masked the underlying signal?

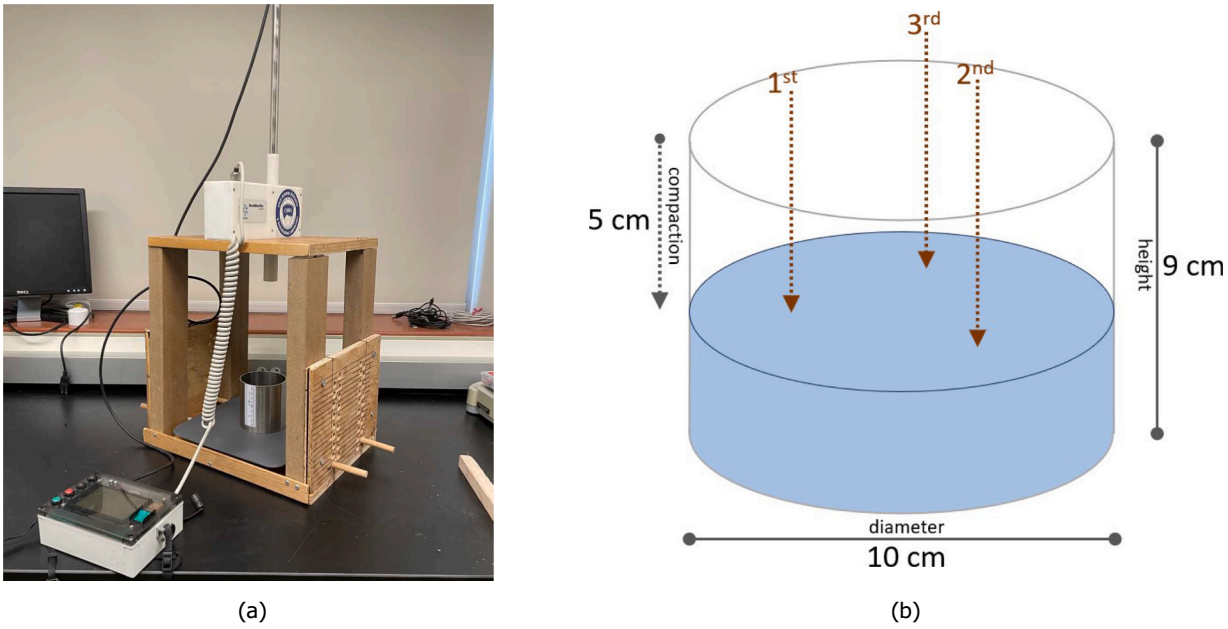

Fig. 4. a) Photo of the SMP on top of the wooden frame. The bottom left side of the photo shows the interface for the SMP. b) The penetration points for the SMP on each sample.

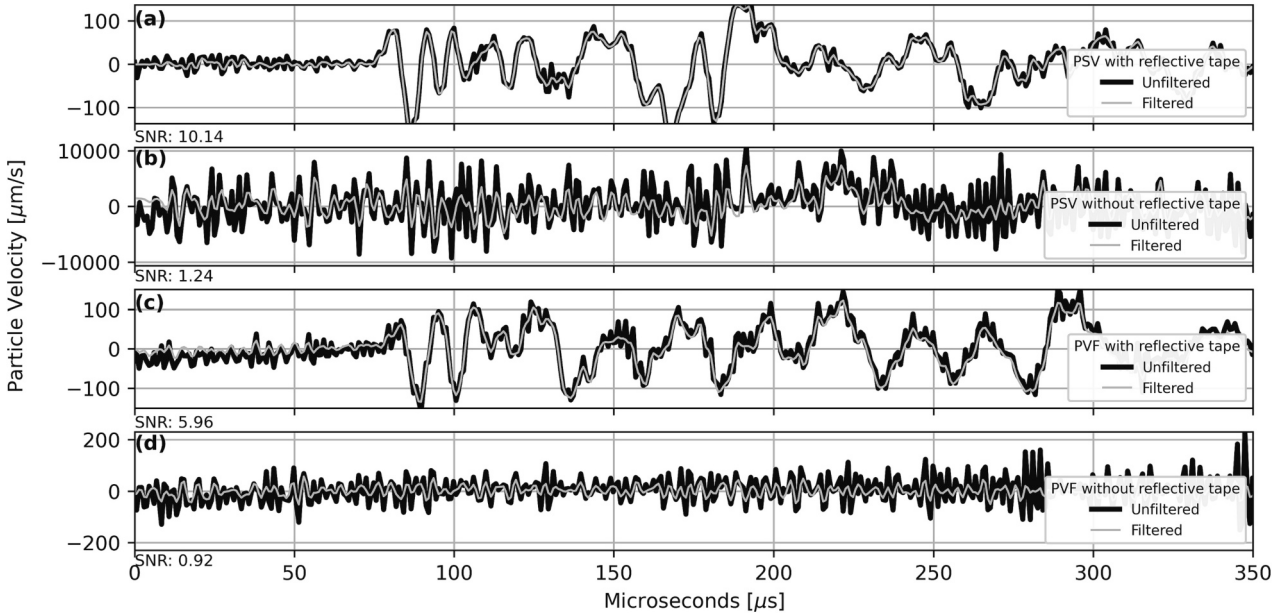

Fig. 5. Each figure contains the raw data (black) overlaid by a cosine tapered and 3–300 kHz bandpass filtered version (gray). (a) PSV time series with reflective tape. (b) PSV time series without reflective tape. (c) PVF time series with reflective tape. (d) PVF time series without reflective tape. The SNR for the filtered data are indicated below each plot. (For interpretation of the references to colour in this figure legend, the reader is referred to the web version of this article.)

The answer is no. In fact, in either system when the surface reflectance values drop below a certain threshold, dropouts in the interference signal occur, leading to high-amplitude spikes in the time-domain signals. If there is a period of low signal return, there is a high probability of a dropout arriving on the decoder inside the laser head. Thus, we can observe that the dropouts are worse for the PSV-400, which is farther away from the sample compared to the PVF and likely has the lower reflectance of the two. In either case, the SNR without tape is ~ 1, which based on how SNR is computed here, means that the noise before and after the P-wave arrival is equivalent.

Our goal in comparing the two laser systems is to determine if either worked without reflective tape given the different standoff distances and other hardware differences within each laser head. It appears that both systems require the tape to capture enough back-scattered light to provide useful ultrasound observations. Additionally, we note that the setup of the two systems was different, with the PVF needing to be placed much closer to the snow surface, which we speculated may have impacted the SNR and eliminated the need for tape. To visualize the differences in two laser systems, we compare the processed time series with reflective tape (Fig. 6). Importantly for this study, the SNR influences our ability to the pick the P-wave first arrival time. Although the first arrival is apparent in both waveforms, the reduced noise in the PSV data prior to the first arrival makes picking the arrival time easier; hence we use the PSV system in the next experiment.

3.2. Compaction experiments

We first calculate the gravimetric density from the measured snow mass and volume at a given compaction (Fig. 7). We also estimate the vertical snow density profile from the SMP data. This estimation process involves a conversion of the observed penetrating force to density via empirical parameterizations. There are four methods to process the SMP data to extract density with the SMP software (Grimm et al., 2018): P2015 (Proksch et al., 2015), CR2020 (Calonne et al., 2020), K2020a (King et al., 2020), and K2020b (King et al., 2020). We compare each method to one another, as well as the gravimetric density (Fig. 7). It is evident that the CR2020 method most closely matches the gravimetric density. Moreover, Calonne et al. (2020) recommends to use CR2020

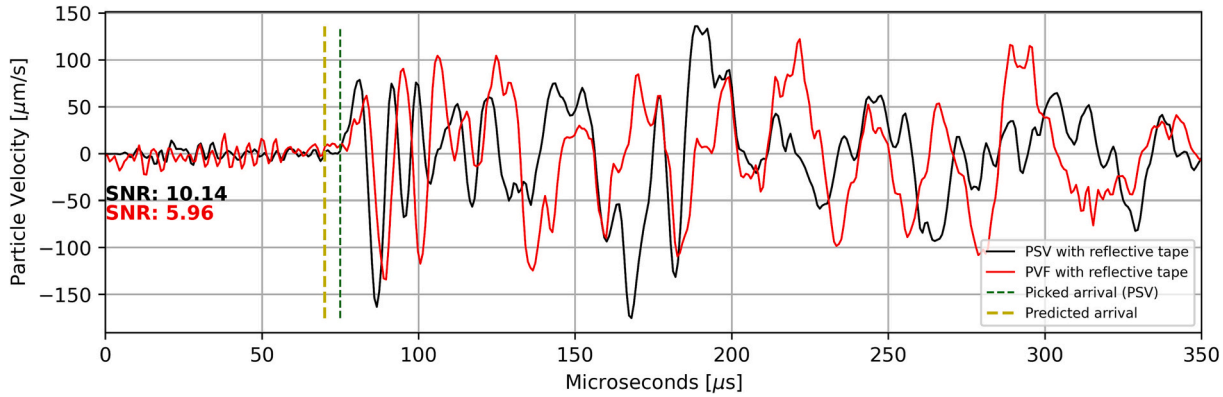

Fig. 6. The PSV (black) and the PVF (red) filtered time series. The P-wave first arrival pick for the PSV is represented by the green dotted line. The two systems have a small variation in arrival times likely due to small differences in the laser receiver spot location during each recording. Noise before the first P-wave arrival is also different in the two systems. These time series are for 1.5 cm compaction with a gravemetric density of 368 kg/m^3. (For interpretation of the references to colour in this figure legend, the reader is referred to the web version of this article.)

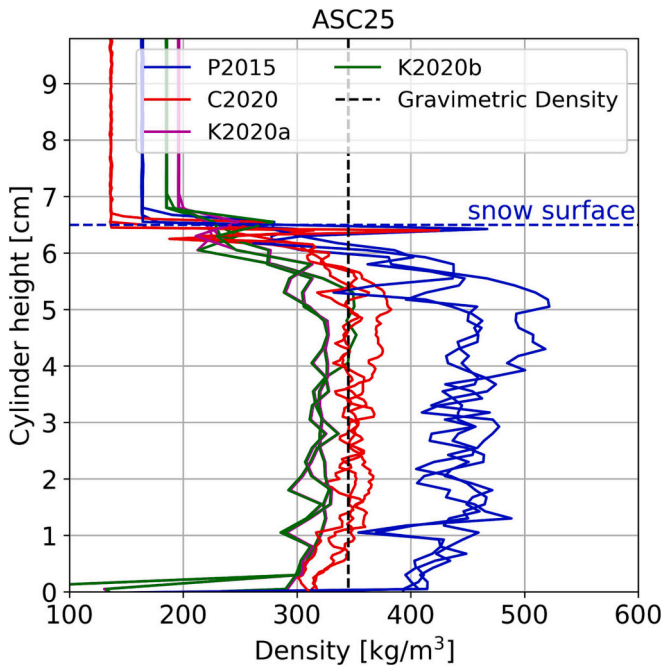

Fig. 7. Comparison of the SMP-density estimation methods: P2015, CR2020, K2020a, and K2020b (see text for more details); the gravimetric density is the black dotted line. The sample is ASC25 (i.e., 2.5 cm compaction) and multiple lines of the same colour indicate multiple SMP runs within that sample.

because this method is parame- terized from the SMP6 hardware (controller Version 4), which is what we used. Thus for the remainder of this study we use the CR2020 density estimation method.

An ideal SMP-density profile is uniform throughout the entire sample depth (e.g., Fig. 8a). However, it is impos- sible to ensure that some samples do not contain compaction bands (Barraclough et al., 2016) due to our compaction process. A noteworthy feature in some SMP-density profiles is a gradual increase in density with depth. This density increase could be due to a high-pressure zone that is created in front of the SMP tip as the cone is pushed into the sample (Marshall and Johnson, 2009). In these instances, we also often observe a drop in the vertical density profile at some point, which exists to the bottom of the sample (e.g., Fig. 8b). This density drop is due to noticeable fracturing within the snow sample and the corresponding reduction in the observed SMP penetration force.

To minimize the impact of vertical and lateral density heterogeneity, the mean SMP density in a compacted sample is computed from all SMP profiles in that sample, but only around the area that the LUS is measured. We compute the mean value and the standard deviation of the SMP density in the interval from 1 cm below the LUS laser spot to 1 cm above the laser spot (i.e., gold shaded area in Fig. 8a and b). This is done for each compaction (Fig. 8c). In general, these mean SMP densities follow a similar trend to the gravimetric densities, and we note that the deviations between the SMP and gravimetric densities range from 1.8 to 29.6% with a mean deviation of 10.7% across all compactions.

That said, we do observe systematic discrepancies at the smallest and largest compactions (i.e., outside of 300–400 kg/m^3). We speculate that these discrepancies can be due to two things. First, it could be that the gravitmetic density is not representative of the actual sample area probed by the LUS due to compaction banding (e.g., Barraclough et al., 2016). Second, the empirical SMP relationships could fail at the extreme density values as these relationships are not necessarily calibrated for the type of snow studied here. Calonne et al. (2020) mentions that the range of validity to this parametrization is not defined due to the absence of measurements under different snowpack conditions, even though data from 70 to 450 kg/m^3 were used to calibrate the model. Given we used shaved ice, it could be that this type of grain is not representative of the snow used in Calonne et al. (2020) across the full range of densities studied here.

For each compacted sample the corresponding PSV ultrasound time series is filtered between 3 and 300 kHz. The first arrival time (t) of the P-wave is picked by hand, and the arrival times are used to compute the *observed wave speed* ($V_o = d/t$), where d is the cylinder diameter (100 mm). We compare this wave speed to the *predicted wave speed* (V_p)

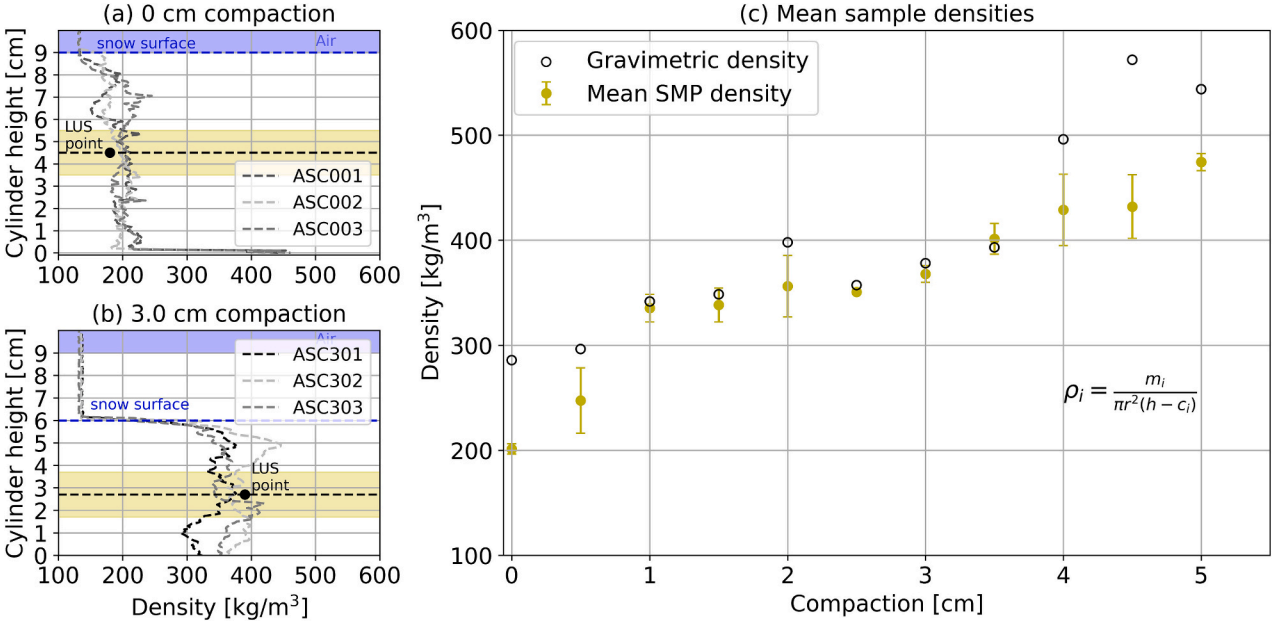

Fig. 8. (a) Example of an ideal SMP measurement – uniform density values throughout the sample. (b) Example of a pressure build up as the SMP penetrates until sample breakage causes a drop in force in the vertical profile and density artificially decreases. (c) Gold dots indicate the mean density for a given compaction sample and bars indicate associated standard deviation. Compaction is the distance the snow sample is compressed from the top of the snow sample cylinder (Fig. 2). Open dots represent the gravimetric density from mass and volume. (For interpretation of the references to colour in this figure legend, the reader is referred to the web version of this article.)

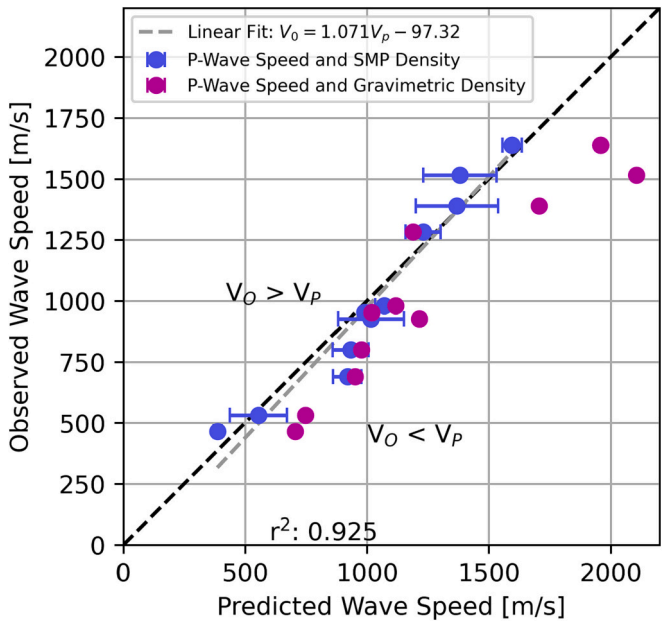

Fig. 9. Comparison of observed (V_o) and predicted (V_p) P-wave speeds. SMP density speeds (blue) and gravimetric density speeds (magenta) are plotted for all compaction samples. Error bars on the P-wave speed are propagated from the SMP density standard deviations. The dashed black line indicates the 1-to-1 wave speed, and the dashed gray line is the least-squares linear fit to the SMP data points (equation in legend), which also has a large r-squared value. (For interpretation of the references to colour in this figure legend, the reader is referred to the web version of this article.)

(Fig. 9), where the predicted wave speed is calculated from Eqs. (3)–(6). We make two wave speed predictions here: 1) using the mean SMP density and 2) using the gravimetric density.

4. Discussion

4.1. PSV vs. PVF

Between the two ultrasound laser experiments, the PSV is the preferred ultrasound laser system for snow in our cold lab setup. This conclusion is due to multiple physical limitations of the PVF laser (e.g., minimum temperature restrictions, standoff distance, and sample sublimation). Furthermore, wavefield datasets for the PSV have a higher SNR due to the stability of the PSV laser head operating outside the cold lab and outside the windy access tube. The.

noise is more pronounced with the VibroFlex Fiber dataset (Fig. 6), so the PSV-400 Scanning Vibrometer dataset has a higher SNR. Polytec Incorporated stipulated the specification not to allow the PVF laser head to reach lower than 0 °C in the rental agreement. This temperature limitation paired with the 0.02 m standoff distance forced us to use the access tube opening next to the optical window (Fig. 10) and allow air flow between the exterior room and cold lab. Unfortunately, the sapphire window has a thickness of 0.025 m and thus the PVF could not be outside the cold lab. The PVF head was fed through the access tube and placed right on the edge to ensure the temperature limit was not crossed. The snow sample was placed just near the access tube opening within the cold lab. Consequently, due the temperature gradient, this configuration created a unidirectional wind flow from outside the cold lab, through the tube, and into the cold lab. This wind caused unwanted vibration along the PVF cable and head. Additionally, and perhaps more importantly, this unidirectional flow caused the snow sample to sublimate, ultimately making the PVF setup an inadequate system due to alteration of the sample over time.

The SNR for the PSV is higher (~2×) than the PVF (Fig. 6). Random noise is observed in both systems, even after stacking 100 traces, and is best observed in the first 70 μs of each trace (Fig. 6). It is also difficult to manually focus the PVF compared to the PSV auto-focus, which makes it much more difficult to obtain the maximum reflectance and thereby leads a lower PVF SNR compared to the PSV. Lastly, when comparing the datasets of both lasers with and without the reflective tape, the reflective tape provides an enhanced SNR. The noise within the datasets, lacking the reflective tape, demonstrates that not enough laser energy is backscattered to observe the actual wavefield. Lastly, some of the noise in the data could be from cold lab vibrations related to the refrigeration system. Future work could temporarily turn off the system while collecting ultrasonic datasets, but in our opinion the reflective tape provides sufficiently strong backscatter.

4.2. Compaction experiments

The predicted P-wave speed and the estimated PSV P-wave speed are similar (Fig. 9). The estimated P-wave speed is obtained from the first-break pick in the ultrasound time series. The predicted P-wave speed is obtained by the empirical model described in Section 2.1. We observe that the predicted wave speed using this model is often greater than the observed wave speed, when using the gravimetric density. We observe that at high wave speed, i.e., at high densities, the predicted wave speed using the gravimetric densities are far from the observed wave speeds. This indicates that perhaps there is compaction banding at high compactions and the gravimentric density does not well represent the sample portion probed by the LUS. Micro X-Ray CT scanning would be one way to investigate this, but we did not have access to such equipment during this study. Thus, using the gravimetric density may not yield reliable wave speed predictions when the possibility for density banding

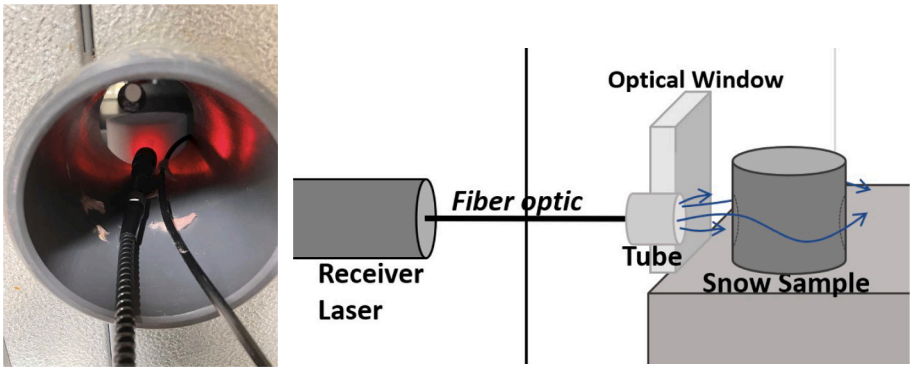

Fig. 10. (a) PVF head within the tube that created the unidirectional flow causing sublimation of snow sample. (b) Diagram describing the sublimation from the unidirectional flow.

exists.

In contrast, the predicted wave speeds using the SMP density around the LUS point fall along the 1-to-1 line. To gauge just how well the SMP-predicted data match the observed data, a linear fit is applied to the SMP data. In general, for this particular snow sample type (i.e., finely shaved ice) the empirical model accurately predicts the fast P-wave speed as indicated by the near parallel linear fit (Fig. 9). We observe that the fit line is very near to the 1-to-1 line, with the mean relative error being 2.7%. This indicates that the coefficients used to predict wave speed for shaved ice are adequate.

The observed P-wave speed and mean SMP density points from of each compacted snow sample are overlain on the compiled dataset of Capelli et al. (2016) (Fig. 11). The predicted P-wave speed is also plotted. These results demonstrate that the observed LUS wave speeds are within the range of the predicted wave speeds for the lab-made shaved-ice snow samples. We note that there is likely some heterogeneity in the density across each snow sample as compaction banding. Moreover, we sample only one LUS point in each snow sample. Thus, we expect some variation in the wave speed and density in space, and we expect that some observed wave speeds do not lie directly on the predicted P-wave speed curve, as also shown in Fig. 9.

Regardless of these small variations, our novel LUS system appears to provide a robust tool to estimate P-wave speed in snow in a non-destructive manner. This tool potentially enables non-destructive lab-based estimation of Young's and shear moduli from P- and S-wave speed information (e.g., Sidler, 2015) in snow samples. Capelli et al. (2016) states that analyzing the properties of acoustic propagation allows for the determination of various mechanical properties of snow, which is possible through analysis of the propagation speed, as demonstrated by Smith (1965) and Takei and Maeno (2004) assuming that the P-wave traveled the fastest path. Additionally, Sidler (2015) states that the stiffness of the snow matrix frame must be greater than that of the pore space, and we must make some assumptions about the homogeneity and isotropy of the sample (e.g., single crystal type, uniform density and porosity, and randomly oriented crystals). Further analysis in this direction using the LUS system is the topic of future research.

Finally, we note that it is apparent in the underlying data complied from past experiments that certain datasets deviate from this predictive model, particularly at high densities. We suspect this model can be improved and that other factors, such as snow crystal type, need to be taken into account. This is the topic of present research and we plan to report on this in the future, now that we have developed a reliable non-destructive LUS for snow characterization.

5. Conclusion

To quantify snow microstructural and mechanical properties in a non-destructive and non-contact manner, we have modified the LUS method of Mikesell et al. (2017) and present a novel method for estimating snow compression wave speed using a non-contacting LUS. The LUS consists of a receiver laser, a source laser, a cold laboratory, and the snow sample. Two receiver laser systems are tested and compared in this study. The results of this ultrasound experiment indicate that the PSV system yields a more robust ultrasound wavefield recording due to the PSV having higher SNR than the PVF in this lab setup. Building on this result, snow compaction experiments are conducted to study P-wave speed as a function of snow density using a poro-elastic model for the interpretation; in this case density is linked to porosity. Geometric parameters of the snow sample are used to calculate the gravimetric density of snow samples, and mean SnowMicroPen (SMP) profiles are used to quantify the spatial variability of snow sample density. The majority of mean SMP density measurements closely match the calculated gravimetric densities with a mean deviation of 10.7%. The P-wave first arrivals estimated from the PSV ultrasound time series are used to compute an observed P-wave speed, which is then compared to the predicted P-wave speed based on the poro-elastic model. The observed P-wave speeds are slightly lower than the predicted P-wave speeds when using the sample-average gravimetric density. The observed wave speed versus SMP density trend matches other snow ultrasound datasets collected using contacting systems (e.g., Capelli et al., 2016). Thus we demonstrate that the non-contacting PSV LUS can replicate previous ultrasound wavefield studies that use contacting systems. This suggests that this novel non-invasive technique can be used for snow studies if reflective tape is adhered to the snow samples. Moreover, the accurate prediction of P-wave speed for shaved-ice snow samples suggests that the poro-elastic theory is adequate to take into account density and porosity, but perhaps not other snow microstructure.

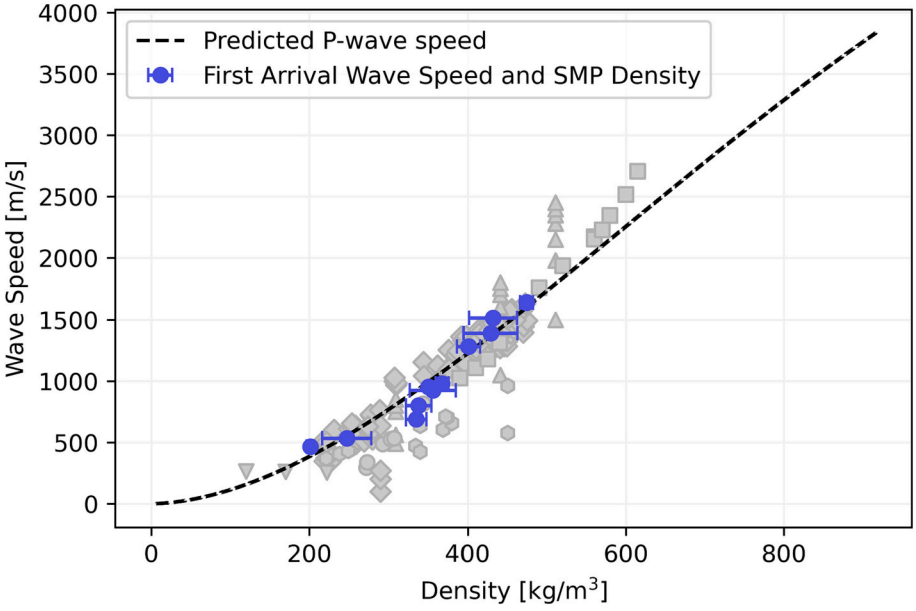

Fig. 11. Observed P-wave speed as a function of mean SMP density (blue dots). The P-wave data compiled by Capelli et al. (2016) are plotted in gray. The predicted P-wave speed (black dashed) is computed from Eqs. (1)–(5). (For interpretation of the references to colour in this figure legend, the reader is referred to the web version of this article.)

CRediT authorship contribution statement

J. Chris McCaslin: Writing – original draft, Visualization, Software, Methodology, Investigation, Formal analysis, Data curation, Conceptualization. **T. Dylan Mikesell:** Writing – review & editing, Validation, Supervision, Resources, Project administration, Methodology, Investigation, Funding acquisition, Formal analysis, Conceptualization. **Hans-Peter Marshall:** Writing – review & editing, Validation, Resources, Conceptualization.

Declaration of competing interest

The authors declare that they have no known competing financial interests or personal relationships that could have appeared to influence the work reported in this paper.

Data availability

All relevant data are presented in the manuscript. Any other details about data or raw data are available upon reasonable request from the corresponding author, as well as codes used in the data analysis.

Acknowledgments

This research is based upon work supported in part by the National Science Foundation under Grant 1906160 and by the Cold Regions Research and Engineering Laboratory (CRREL). JCM is supported by the SMART Scholarship funded by: OUSD/R&E (the Under Secretary of Defense Research and Engineering), National Defense Education Program (NDEP)/BA-1, Basic Research. We thank Achille Capelli for providing the past ultrasound data presented here. We also thank the Associate Editor, Nicolas Eckert, and two anonymous reviewers whose constructive feedback improved the quality of this manuscript. Finally, we thank Vicki Lu from Polytec GmbH for training on the use of the PVF system and answering all our questions.

References

Barraclough, T.W., Blackford, J.R., Liebenstein, S., Sandfeld, S., Stratford, T.J., Weinländer, G., Zaiser, M., 2016. Propagating compaction bands in confined compression of snow. Nat. Phys. 13, 272–275.

Brucker, L., Picard, G., Arnaud, L., Barnola, J., Schneebeli, M., Brunjail, H., Lefebvre, E., Fily, M., 2011. Modeling time series of microwave bright- ness temperature at Dome C, Antarctica, using vertically resolved snow temperature and microstructure measurements. J. Glaciol. 57 https://doi.org/10.3189/002214311795306736.

Calonne, N., Richter, B., Löwe, H., Cetti, C., Schure, J., Herwijnen, A.V., Fierz, C., Jaggi, M., Schneebel, M., 2020. The RHOSSA campaign: multi-resolution monitoring of the seasonal evolution of the structure and mechanical stability of an alpine snowpack. Cryosphere 14, 1829–1848. https://doi.org/10.5194/tc-14-1829-2020.

Capelli, A., Kapil, J.C., Reiweger, I., Or, D., Schweizer, J., 2016. Speed and attenuation of acoustic waves in snow: Laboratory experiments and modeling with Biot's theory. Cold Reg. Sci. Technol. 125, 1–11. https://doi.org/10.1016/j.coldregions.2016.01.004.

Carcione, J.M., Picotti, S., 2006. P-wave seismic attenuation by slow-wave diffusion: Effects of inhomogeneous rock properties. Geophysics 71, O1–O8.

Fellah, Z.E.A., Berger, S., Lauriks, W., Depollier, C., Aristegui, C., Chapelon, J., 2003a. Measuring the porosity and the tortuosity of porous materials via reflected waves at oblique incidence. J. Acoust. Soc. Am. 113, 2424–2433. https://doi.org/10.1121/1.1567275.

Fellah, Z.E.A., Berger, S., Lauriks, W., Depollier, C., Trompette, P., Chapelon, J., 2003b. Ultrasonic measurement of the porosity and tortuosity of air-saturated random packings of beads. J. Acoust. Soc. Am. 113, 9352–9359. https://doi.org/10.1063/1.1572191.

Grimm, S., Löwe, H., Theile, T., Schoch, M., Reisecker, M., 2018. Snowmicropyn python package https://snowmicropyn.readthedocs.io/en/latest/overview.html.

Gubler, H., 1977. Artificial release of avalanches by explosives. J. Glaciol. 19, 419–429. https://doi.org/10.3189/S0022143000029440.

Gubler, H., 1983. Remote instrumentation for avalanche warning systems and snow cover monitoring. J. Glaciol. 137–142.

Gudra, T., Najwer, L., 2011. Ultrasonic investigation of snow and ice parameters. Opt. Acoust. Methods Sci. Technol. 120, 625–629.

Hariharan, P., 2006. Basics of Interferometry, 2nd edition. Academic Press.

Herwijnen, A.V., Schweizer, J., 2011. Monitoring avalanche activity using a seismic sensor. Cold Reg. Sci. Technol. 69, 165–176. https://doi.org/10.1016/j.coldregions.2011.06.008.

Hofstede, C., Eisen, O., Diez, A., Jansen, D., Kristoffersen, Y., Lambrecht, A., Mayer, C., 2013. Investigating englacial reflections with vibro- and explosive-seismic surveys at Halvfarryggen ice dome, Antarctica. Ann. Glaciol. 54, 189–200. https://doi.org/10.3189/2013AoG64A064.

Ishida, T., 1965. Acoustic properties of snow. Contrib. Inst. Low Temp. Sci. Ser. 20, 23–63.

Iwase, T., Sakuma, T., Yoshihisa, K., 2001. Measurements on sound propagation characteristics in snow layer. In: Alippi, A. (Ed.), 17th International Congress on Acoustics ICA 17, pp. 23–63.

Johnson, J., 1982. On the application of biot's theory to acoustic wave propagation in snow. Cold Reg. Sci. Technol. 6, 49–60.

Kapil, J., Datt, P., Kumar, A., Singh, K., Kumar, V., Satyawali, P., 2014. Multi-sensor couplers and waveguides for efficient detection of acoustic emission behavior of snow. Cold Reg. Sci. Technol. 101, 1–13. https://doi.org/10.1016/j.coldregions.2014.01.003.

Kinar, N.J., Pomeroy, J.W., 2009. Automated determination of snow water equivalent by acoustic reflectometry. IEEE Trans. Geosci. Remote 47, 1–19. https://doi.org/10.1109/TGRS.2009.2019730.

King, J., Howell, S., Brady, M., Toose, P., Derksen, C., Haas, C., Beckers, J., 2020. Local-scale variability of snow density on Arctic Sea ice. Cryosphere 14, 4323–4339. https://doi.org/10.5194/tc-14-4323-2020.

Lacroix, P., Grasso, J.R., Roulle, J., Giraud, G., Goetz, D., Morin, S., 2012. Monitoring of snow avalanches using a seismic array: location, speed estimation, and relationships to meteorological variables. J. Geophys. Res. Earth 117, F01034. https://doi.org/10.1029/2011JF002106.

Lieblappen, R., Fegyveresi, J.M., Courville, Z., Albert, D.G., 2020. Laser ultrasound observations of mechanical property variations in ice cores. Front. Earth Sci. 8, 1–11. https://doi.org/10.3389/feart.2020.00034.

Lowe, H., Herwijnen, A., 2012. A Poisson shot noise model for micro-penetration of snow. Cold Reg. Sci. Technol. 70, 62–70. https://doi.org/10.1016/j.coldregions.2011.09.001.

Marco, O., Buser, O., Villemain, P., Touvier, F., Revol, H., 1998. Acoustic impedance measurement of snow density. Ann. Glaciol. 26, 92–96.

Marshall, H.P., Johnson, J.B., 2009. Accurate inversion of high-resolution snow penetrometer signals for microstructural and micromechanical properties. J. Geophys. Res. 114, 1–18. https://doi.org/10.1029/2009JF001269.

Mason, W.P., Thurston, R.N., 1972. Physical Acoustics Principles and Methods. Academic Press Inc. IX.

Mavko, G., Mukerji, T., Dvorkin, J., 2020. The Rock Physics Handbook. Cambridge university press.

McGrath, D., Bonnell, R., Zeller, L., Bump, A.O.M.E., Webb, R., Marshall, H.P., 2022. A time-series of snow density and snow water equivalent observations de- rived from the integration of gpr and uav sfm observations. Front. Remote Sens. 3 https://doi.org/10.3389/frsen.2022.886747.

Mikesell, T.D., Wijk, K.V., Otheim, L.T., Marshall, H.P., Kurbatov, A., 2017. Laser ultrasound observations of mechanical property variations in ice cores. Geosciences (Switzerland) 7, 1–19. https://doi.org/10.3390/geosciences7030047.

Oura, H., 1952. Snow velocity in the snow cover. Contrib. Inst. Low Temp. Sci. Ser. A9, 171–178.

Picard, G., Lowe, H., Domine, F., Arnaud, L., Larue, F., Favier, V., Meur, E.L., Lefebvre, E., Savarino, J., 2022. The Microwave Snow Grain size: a New Concept to Predict Satellite Observations over Snow-Covered Regions. AGU Adv. 3, 1–19. https://doi.org/10.1029/2021AV000630.

Polytec, 2022. VibroFlex Fiber Datasheet. URL: https://www.polytec.com/eu/vibrometry/products/single-point-vibrometers/vibroflex.

Proksch, M., Löwe, H., M.S, 2015. Density, specific surface area, and correlation length of snow measured by high-resolution penetrometry. JGR Earth Surf. 120, 1–19. https://doi.org/10.1002/2014JF003266.

Reiweger, I., Mayer, K., Steiner, K., Dual, J., Schweizer, J., 2015. Measuring and localizing acoustic emission events in snow prior to fracture. Cold Reg. Sci. Technol. 110, 160–169. https://doi.org/10.1016/j.coldregions.2014.12.002.

Ruiz, J.J., Vehmas, R., Lemmetyinen, J., Uusitalo, J., Lahtinen, J., Lehtinen, K., Kontu, A., Rautiainen, K., Tarvainen, R., Pulliainen, J., Praks, J., 2020. SodSAR: a tower-based 1–10 GHz SAR system for snow, soil and vegetation studies. MDPI Sens. 20, 1–18. https://doi.org/10.3390/s20226702.

Schneebeli, M., Johnson, J., 1999. Measuring snow microstructure and hardness using a high resolution penetrometer. Cold Reg. Sci. Technol. 30, 101–114. https://doi.org/10.1016/S0165-232X(99)00030-0.

Scruby, C.B., Drain, L.E., 1990. Laser Ultrasonics: Techniques and Applications. Adam Hilger, New York.

Shapiro, L.H., Johnson, J.B., Sturm, M., Blaisdell, G.L., 1997. Snow Mechanics: Review of the State of Knowledge and Applications. CRREL Technical Report.

Shoop, S.A., Bodie, M.O., Frankenstein, S., Bigl, M.F., 2020. Recent improvements to snow mobility algorithms.

Sidler, R., 2015. A porosity-based Biot model for acoustic waves in snow. J. Glaciol. 61, 789–798.

Smith, J., 1965. The Elastic Constants, Strength and Density of Greenland Snow as Deter-Mined from Measurements Ofsonic Wave Velocity. CRREL Technical Report 167. U. S.A, US Army Cold Regions Research and Engineering Laboratory, Hanover NH.

Smith, N., 1969. Determining the Dynamic Properties of Snow and Ice by Forced Vibration, vol. 216. US Army Materiel Command, Terrestrial Sciences Center, Cold Regions Research.

Sopher, A., Shoop, S., 2017. Stress analysis of the phoenix compacted snow runway to support wheeled aircraft. In: *Congress on Technical Advancement 2017*, pp. 161–172.

Stefko, M., Leinss, S., Frey, O., Hajnsek, I., 2022. Coherent backscatter enhancement in bistatic Ku- and X-band radar observations of dry snow. Cryosphere 16, 2859–2879.

Surinach, E., Furdada, G., Sabot, F., Biesca, B., Vilaplana, J., 2001. On the characterization of seismic signals generated by snow avalanches for monitoring purposes. Ann. Glaciol. 32, 268–274. https://doi.org/10.3189/172756401781819634.

Takei, I., Maeno, N., 2004. Mechanical vibration responses of snow samples near the melting temperature. Ann. Glaciol. 38, 130–134. https://doi.org/10.3189/172756404781815022.

Tsang, L., Durand, M., Derksen, C., Barros, A.P., Kang, D., Lievens, H., Marshall, H.P., Zhu, J., Johnson, J., King, J., Lemmetyinen, J., Sandells, M., Rutter, N., Siqueira, P., Nolin, A., Osmanoglu, B., Vuyovich, C., Kim, E., Taylor, D., Merkouriadi, I., Brucker, L., Navari, M., Dumont, M., Kelly, R., Kim, R.S., Liao, T.H., Borah, F., Xu, X., 2022. Review article: Global monitoring of snow water equivalent using high-frequency radar remote sensing. Cryosphere 16, 3531–3573. https://doi.org/10.5194/tc-16-3531-2022.

Yamada, T., Hasemi, T., Izumi, K., Sat, A., 1974. On the dependencies of the velocities of P- and S- waves thermal conductivity of snow upon the texture of snow. Contrib. Inst. Low Temp. Sci. Ser. 32, 71–80.